REPORT DOCUMENTATION PAGE

1. REPORT DATE *(DD-MM-YYYY)* 16/08/2016	2. REPORT TYPE Final Report	3. DATES COVERED *(From - To)* 6/15/2012 – 9/15/2015

4. TITLE AND SUBTITLE
"Sea Spray Generation at a Rocky Shoreline"

5a. CONTRACT NUMBER
N00014-12-C-0290

5b. GRANT NUMBER

5c. PROGRAM ELEMENT NUMBER

6. AUTHOR(S)
Edgar L Andreas

5d. PROJECT NUMBER

5e. TASK NUMBER

5f. WORK UNIT NUMBER

7. PERFORMING ORGANIZATION NAME(S) AND ADDRESS(ES)

NorthWest Research Associates
PO Box 3027
Bellevue, WA 98009-3027

8. PERFORMING ORGANIZATION REPORT NUMBER
R135 – ONR S068P

9. SPONSORING / MONITORING AGENCY NAME(S) AND ADDRESS(ES)
Office of Naval Research
Attn: Dr. Scott Harper, ONR 322

875 North Randolph St
Arlington, VA 22203-1995

10. SPONSOR/MONITOR'S ACRONYM(S)

11. SPONSOR/MONITOR'S REPORT NUMBER(S)

12. DISTRIBUTION / AVAILABILITY STATEMENT

Distribution Statement A. Approved for public release; distribution is unlimited.

13. SUPPLEMENTARY NOTES

14. ABSTRACT

This Abstract is written by Dr. Joan Oltman-Shay, President of NWRA, on behalf of Dr. Ed Andreas, the PI on this project. Dr. Andreas worked on this project until his untimely death in late September 2015. A month earlier, he had just completed and submitted to the American Meteorology Society journal a paper representing and acknowledging work on this project. The paper, "Sea Spray Generation at Rocky Shoreline" by Ed Andreas was accepted for publication and as of July 2016 was being processed for publication.

15. SUBJECT TERMS
Need a few terms here

16. SECURITY CLASSIFICATION OF:			17. LIMITATION OF ABSTRACT	18. NUMBER OF PAGES	19a. NAME OF RESPONSIBLE PERSON
a. REPORT Unclassified	**b. ABSTRACT** Unclassified	**c. THIS PAGE** Unclassified	U	49	**19b. TELEPHONE NUMBER** *(include area code)* 425-556-9055

1
2
3
4
5
6
7
8
9
10
11
12
13

Sea Spray Generation at a Rocky Shoreline

14
15
16
17

Edgar L Andreas
18
19
NorthWest Research Associates, Inc.
Lebanon, New Hampshire
20
21

22
23
24
25
26
27
28
29
30
31
32
33
34

35 *Corresponding author address:* Dr. Edgar L Andreas, NorthWest Research Associates, Inc.,
36 25 Eagle Ridge, Lebanon, NH 03766-1900.
37 E-mail: eandreas@nwra.com

38
39
40
41 July 2015

42   ABSTRACT

43   With sea ice in the Arctic continuing to shrink, the Arctic Ocean and the surrounding

44   marginal seas will become more like the ocean at lower latitudes. In particular, with more open

45   water, air-sea exchange will be more intense, and storms will be stronger and more frequent.

46   The longer fetches over open water and the more energetic storms will combine to produce

47   higher waves and more sea spray. Offshore structures—such as oil drilling, exploration, and

48   production platforms—will face increased hazards from freezing sea spray.

49   Based on sea spray observations made with a cloud imaging probe at Mt. Desert Rock, an

50   island off the coast of Maine, I quantify the spray that artificial islands built in the Arctic might

51   experience. Mt. Desert Rock is small, low, unvegetated, and has an abrupt, rocky shoreline like

52   these artificial islands. Many of the observations were at air temperatures below freezing. This

53   paper reports the near-surface spray concentration and the rate of spray production at this rocky

54   shoreline for spray droplets with radii from 6.25 to 143.75 µm and for wind speeds from 5 to

55   17 m s^{-1}. Spray concentration increases as the cube of the wind speed, but the shape of the

56   concentration spectrum with respect to radius does not change with wind speed. Both near-

57   surface spray concentration and the spray production rate are three orders of magnitude higher at

58   this rocky shoreline than over the open ocean because of the high energy and resulting

59   continuous white water in the surf zone.

60

1. Introduction

With the Arctic sea ice retreating farther and farther each summer, the Arctic Ocean is beginning to take on characteristics of the ocean at lower latitudes. In particular, heat lost from the now-open ocean can lead to more intense mesoscale storms; and the combination of storm winds and longer open water fetches will produce higher waves (e.g., Perrie et al. 2012; Asplin et al. 2012). Such evolving conditions will present new hazards for artificial structures like semi-submersible drilling rigs and man-made islands used as oil exploration and production platforms (Jones and Andreas 2009). Although the wind and waves themselves will create hazards for these structures, my interest here is the attendant sea spray produced.

Jones and Andreas (2009, 2012) previously considered the spray icing of semi-submersible drilling platforms that had fairly open profiles at the waterline such that most of the spray resulted from breaking waves in open water (also Minsk 1984a; Nauman 1984). Here, I turn to spray effects that small, artificial islands built in the Arctic Ocean can face: spray largely created by waves breaking along their shoreline. At sub-freezing temperatures, such spray will accumulate as ice on virtually all surfaces on these small islands (e.g., Minsk 1984b; Itagaki 1984). Even in above-freezing temperatures, the sea salt generated by high wind and waves will collect on raised structures and speed the corrosion of metal surfaces.

To quantify the rate of such shore-induced spray production, I carried out a month-long experiment in January 2013 on Mt. Desert Rock, an unvegetated island with low relief 24 miles out to sea from Bar Harbor, Maine. Mt. Desert Rock has a size and a topographic profile that is similar to some of the artificial islands now in the Arctic (e.g., Muzik and Kirby 1992; Gerwick 2007, Chapter 23). I presume that the spray concentrations and generation rates observed on Mt. Desert Rock will be similar to the values near other rocky shorelines and, in particular, will be

84   what artificial islands in the Arctic might experience in the coming decades.

85   Although the literature contains several papers that report sea spray observations at

86   shorelines, my data are unique in several ways. Climatologically, Mt. Desert Rock in January

87   provides a good chance of encountering sub-freezing air temperatures and winds high enough to

88   produce copious spray. And, indeed, roughly half of my measurements were made at

89   temperatures below freezing. I am unaware of other spray data collected at temperatures below

90   freezing.

91   Secondly, most of the previous spray measurements from the coastal zone looked at only

92   relatively small droplets. For example, de Leeuw et al. (2000), Vignati et al. (2001), Clarke et al.

93   (2006), van Eijk et al. (2011), and Piazzola et al. (2015) all reported recent spray observations in

94   coastal regions, and all sampled droplets with radii at formation as small as 0.02 to 0.1 µm. Only

95   van Eijk et al., however, sampled droplets with radii up to about 30 µm; the other papers

96   reported on droplets with radii up to only 10–20 µm. While these small droplets are plentiful,

97   they do not carry enough mass to produce the severe icing that larger droplets do (Jones and

98   Andreas 2012).

99   Therefore, on Mt. Desert Rock, I collected spray data with a cloud imaging probe for

100   which the smallest radius bin was centered at 6.25 µm and the instrument was capable of

101   counting droplets with radii up to 775 µm. Although the counting statistics were poor for the

102   largest droplets, I do report here spray concentration measurements for droplets in a radius bin

103   centered at 143.75 µm—well into what is referred to as the *spume* regime for open ocean spray.

104   Thus, I believe these observations represent the largest spray droplets that have been measured

105   near a shoreline.

106   In this paper, I report data from the cloud imaging probe deployed for 27 days near the

107   shoreline on Mt. Desert Rock. These data span 12.5-μm-wide radius bins with centers ranging

108   from 6.25 to 143.75 μm and include 10-m winds from 5 to 17 m s^{-1}. A key finding is that the

109   droplet spectra have the same shape at all observed wind speeds. I am thus able to derive an

110   expression for the near-surface droplet concentration as the product of a function of just droplet

111   radius and another function that goes as the cube of the wind speed. This concentration function,

112   lastly, yields a function for predicting spray generation when ocean waves encroach on a rocky

113   (as opposed to a sloping, sandy) shoreline.

114

2. Measurements on Mt. Desert Rock

Mt. Desert Rock, 24 miles into the Atlantic east of Bar Harbor, Maine, has a lightkeeper's house and a stone lighthouse that NOAA has instrumented as a C-MAN station under the National Data Buoy Center (NDBC). The College of the Atlantic in Bar Harbor owns Mt. Desert Rock and, as such, facilitates access to the "Rock" and provided us logistics support.

Figure 1 shows how small Mt. Desert Rock is and identifies the permanent structures there and the 2013 instrument locations. The "Rock" is truly a desert island: Its surface has no vegetation but is simply a rocky outcrop. From our survey (these numbers may differ from the NDBC information), the high point of the island is only 9.2 m above mean sea level; the lighthouse is 18 m tall. Prevailing winds at Mt. Desert Rock in January are westerly and northwesterly. We placed all instruments for best exposure to these winds.

To provide a rigid base and some security for the expensive cloud imaging probe (CIP; from Droplet Measurement Technologies), we mounted it on the foghorn platform (Fig. 1). As such, the probe was 3.24 m above local ground and 8.66 m above mean sea level. Because the wind speed and direction through the probe's laser array are crucial for computing spray concentration, the cloud imaging probe was rigidly attached to a Gill WindMaster sonic anemometer/thermometer (Fig. 2). The sonic's sample area was 0.48 m above the CIP's laser array. We frequently rotated this whole system to orient the cloud imaging probe into the wind. The appendix summarizes the equations that I used for obtaining spray concentration from the CIP.

To document near-surface meteorological conditions during our measurements, we deployed a "turbulence tripod" near the high-water line (Fig. 1). This tripod held a three-axis sonic anemometer/thermometer from Applied Technologies, Inc. (ATI), 2.35 m above ground, a

138   Li-Cor water vapor and carbon dioxide sensor 2.10 m above ground, and an Ophir hygrometer

139   (which also measured air temperature) 2.23 m above ground. The ground here was 4.4 m above

140   mean sea level.

141   I supplemented our own measurements with the NOAA measurements from the Mt.

142   Desert Rock lighthouse; from another NOAA C-MAN station on nearby Matinicus Rock; and

143   from two nearby buoys, 44034 and 44037, owned and maintained by the Northeastern Regional

144   Association of Coastal Ocean Observing Systems.

145   Figures 3 and 4 show time series of meteorological and oceanographic data for January

146   2013 from these various sources. The winds denoted "MDR NOAA" and "Matinicus" were

147   measured by the C-MAN instruments high on the Mt. Desert Rock and Matinicus lighthouses,

148   respectively, and thus show higher speeds than the measurements nearer the surface from the two

149   buoys and from the ATI and Gill sonics. These latter data are more representative of the wave

150   and spray conditions and show that we sampled in winds up to about 17 m s^{-1}. The temperature

151   panel in Fig. 3 shows that air temperatures were always less than 10°C during the measurements

152   and were frequently below freezing. The stratification was generally unstable (water warmer

153   than air; Figs. 3 and 4).

154

3. Data analysis

155

156   The appendix reviews the equations I used for processing measurements from the cloud

157   imaging probe. Briefly, I computed spray concentrations in 12 radius bins, each 12.5-μm wide,

158   from zero to 150 μm. The center radius in each bin locates the bin average in the upcoming plots

159   and calculations.

160   The cloud imaging probe ran continuously, except when we stopped recording to reorient

161   it into the wind. As such, from its 1 Hz measurements, I computed half-hour averages of spray

162   concentrations for the first 30 minutes of an hour and for the second 30 minutes. For instances

163   when the recording did not start at the top of the hour or end exactly at the top of the hour, I still

164   computed averages from these partial 30-minute runs. I did, however, later exclude runs that

165   were shorter than 15 minutes.

166   For the CIP site on Mt. Desert Rock, the counting statistics for the largest bins that the

167   cloud imaging probe could sample were poor. Hence, the bin centered at a radius of 143.75 μm

168   was the largest one that I retained for analysis. Moreover, for any bin, I retained its average only

169   if it had counted at least ten droplets during the averaging period.

170   The Gill sonic anemometer attached to the cloud imaging probe sampled the three wind

171   components and the sonic temperature roughly six times per second. I averaged these data over

172   the same averaging periods as for the CIP. From the average along-wind ($\overline{U}$) and cross-wind

173   ($\overline{V}$) components, I could compute the wind's average attack angle into the laser array of the

174   cloud imaging probe. If this attack angle is not small, droplets hitting the thin arms that extend

175   from the body of the CIP and hold the laser array (Fig. 2) can shatter; and the resulting smaller

176   droplets can pass through the array and be counted. To minimize these erroneous counts, I kept

177   for analysis only runs for which the attack angle of the wind was between –20° and +20°.

7

178   From $\overline{U}$, $\overline{V}$, and a measurement of the CIP's angular orientation, I also calculated the

179   wind direction at the CIP in a true-north coordinate system. Figure 1 shows that for wind

180   directions between 260° and 7° the CIP had best exposure to the ocean. My analysis includes

181   only runs for which the average wind direction at the CIP was in this sector.

182   I also sequenced the analysis with the nearest tidal record, from Bar Harbor (NDBC

183   station 8413220), and thereby assigned each half-hour run a tidal height. The arcs at 50 and

184   75 m in Fig. 1 show that, at high tide, the cloud imaging probe was well within 50 m of open

185   water. Even at low tide, it was no more than about 75 m from open water and was often much

186   closer.

187   Nevertheless, to judge whether distance from the water affected the spray counts,

188   subsequent plots distinguish between the data collected during high water and low water. The

189   tidal range during our observations was –0.43 to 3.93 m. Therefore, I designate as *low water*

190   runs those collected when the tide was between –0.43 and 1.75 m; *high water* runs were

191   collected when the tide was between 1.75 m and 3.93 m.

192   For measurements over the ocean, the neutral-stability wind speed at 10 m, U_{N10}, is

193   commonly the independent variable in analyses and plots. I obtained U_{N10} from the Gill sonic.

194   Its measurements of the three wind components yielded U_z, the average wind speed at height z_s

195   for each half-hour CIP run. Similarity theory (e.g., Panofsky and Dutton 1984, p. 134) then

196   relates U_z to the wind speed at 10 m:

197
$$U_{10} = U_z + \frac{u_*}{k}\left[\ln\left(\frac{10}{z_s}\right) - \psi_m\left(\frac{10}{L}\right) + \psi_m\left(\frac{z_s}{L}\right)\right].$$
(3.1)

198   Here, u_* is the friction velocity; k (= 0.40) is the von Kármán constant; z_s (= 3.72 m) is the height

199   of the Gill sonic above the local surface; and ψ_m is a stratification correction that is a function of

8

200   the Obukhov length, L.

201   Because, in subsequent analyses I ignore runs for which the 10-m wind speed was less

202   than 5 m s^{-1} (because there was negligible spray) and because z_s and 10 m are relatively small, I

203   ignore the stratification corrections in (3.1) because they are small. Hence, (3.1) yields a simpler

204   expression for U_{N10}:

205     $$U_{N10} \ = \ U_z \ + \ \frac{u_*}{k}\ln\left(\frac{10}{z_s}\right).$$ (3.2)

206   Meanwhile, Andreas et al. (2012) deduced a relationship between u_* and U_{N10} from

207   several thousand observations over the open ocean:

208     $$u_* \ = \ 0.239 + 0.0433\left\{(U_{N10} - 8.271) + \left[0.120(U_{N10} - 8.271)^2 + 0.181\right]^{1/2}\right\}.$$ (3.3)

209   Here, both u_* and U_{N10} are in m s^{-1}. Substituting (3.3) for u_* in (3.2) yields a single equation that

210   relates the measurement, U_z, to the desired quantity, U_{N10}. I solved it using Newton's method

211   and thereby obtained values for both U_{N10} and u_* for each CIP run.

212   To standardize the spray concentrations to a common height that will also be relevant for

213   estimating the spray generation function, I extrapolated the spray observations to the height of

214   the wave crests. I designate these concentrations C_0 and interpret them as the concentration at

215   the sea surface (e.g., Fairall et al. 2009; Andreas et al. 2010). Fairall et al. (2009) used the

216   following relation to convert the spray concentration at height z_1 to the concentration at height z_2:

217     $$C(z_2, r_0) \ = \ C(z_1, r_0)\left(\frac{z_2}{z_1}\right)^{-V_g(r_0)/k\,u_*\,f_s}.$$ (3.4)

218   Here, both concentrations are for droplets with a radius at formation of r_0, $V_g(r_0)$ is the terminal

219   fall speed of these droplets, and f_s is related to the turbulent diffusivity of the droplets.

220   Because I want to estimate C_0, z_2 becomes $H_{1/3}/2$ ($= A_{1/3}$), the significant wave amplitude,

9

221   where $H_{1/3}$ is the significant wave height (Fig. 4). In other words, z_2 is the average height above

222   mean sea level of the wave crests. Fairall et al. (2009), among others, assume that $C(z_2,r_0)$ is

223   constant between $A_{1/3}$ and the mean water surface. Consequently, $C(A_{1/3},r_0)$ is a reasonable

224   estimate for C_0. As such, (3.4) becomes

$$C_0(r_0) = C(z_{CIP},r_0)\left(\frac{A_{1/3}}{z_{CIP}}\right)^{-V_g(r_0)/k\,u_*\,f_s} , \qquad (3.5)$$

226   where z_{CIP} is the height of the cloud imaging probe above the local surface.

227   For f_s in (3.5), I use (Rouault et al. 1991; Kepert et al. 1999; Fairall et al. 2009)

$$f_s(r_0,u_*) = \frac{1}{1+2\left[V_g(r_0)/\sigma_w\right]^2} , \qquad (3.6)$$

229   where σ_w is the standard deviation of the vertical velocity fluctuations of the air. Continuing

230   with the assumption of near-neutral-stratification, I use for σ_w in (3.6) 1.25 u_* (Kaimal and

231   Finnigan 1994, p. 16).

232   Lastly, $A_{1/3}$ in (3.5) comes from the algorithm that Andreas and Wang (2007) derived

233   from data collected by NDBC buoys off the northeast coast of the United States, including

234   several in the vicinity of Mt. Desert Rock. Figure 4 compares the estimates of $H_{1/3}$ from this

235   algorithm with the data from buoys 44034 and 44037. Agreement between the Andreas and

236   Wang algorithm and the buoy data is generally good, but the Andreas and Wang algorithm does

237   predict a non-zero lower limit for $H_{1/3}$ in light winds. This lower limit is obvious in Fig. 4 but is

238   not an issue for this analysis because it occurs when the wind speed was less than 5 m s^{-1}, and I

239   ignore these wind speeds in the upcoming results.

240

241 **4. Sea spray concentration**

242   Figures 5 and 6 show the near-surface spray droplet concentration spectra (i.e., C_0) as

243 measured by the cloud imaging probe. Each panel breaks out measurements for wind speeds

244 (U_{N10} in this case) in ranges between 6 and 17 m s^{-1}. Each panel also identifies measurements

245 made during high water and low water.

246   Figures 5 and 6 do not reveal any obvious differences between the measurements made

247 during high water and low water. Both the magnitude of the concentrations and the shape of the

248 spectra as a function of radius are similar for the two types of observations.

249   In fact, in Figs. 5 and 6, the spectral shape seems to be the same for all wind speeds. I

250 therefore nondimensionalized all the spectra in Figs. 5 and 6 with the concentration measured at

251 $r_0 = 6.25$ µm for each spectrum. Figure 7 plots nondimensional versions of all 363 spectra

252 collected in wind speeds of 5 m s^{-1} and higher. Still here, the figure distinguishes the 170 spectra

253 collected during high water from the 163 spectra collected during low water to reiterate that the

254 distance to open water does not seem to have influenced the results. That is, the medians for all

255 the data in a radius bin and the medians for just the high water and low water observations in a

256 bin are all largely indistinguishable.

257   The four small-radius bins in Fig. 7 fall on a straight line on this log-log plot,

258 $$\ln\left[C_0(r_0)/C_0(r_0=6.25\mu m)\right] = 3.39396 - 1.85201\ln(r_0); \qquad (4.1)$$

259 the six large-radius bins similarly fall along another straight line,

260 $$\ln\left[C_0(r_0)/C_0(r_0=6.25\mu m)\right] = 21.71391 - 6.31974\ln(r_0). \qquad (4.2)$$

261 I can therefore derive a hyperbola to fit the entire nondimensional spectrum,

11

$$\ln\left[C_0\left(r_0\right)/C_0\left(r_0=6.25\mu\text{m}\right)\right] = -4.20022$$

262

$$-4.08587\left\{\left[\ln\left(r_0\right)-4.10051\right]+\left\{0.29891\left[\ln\left(r_0\right)-4.10051\right]^2+0.78383a^2\right\}^{1/2}\right\}. \qquad (4.3)$$

263   Here, a is a coefficient that moves the knee of the hyperbola as close to the intersection of lines

264   (4.1) and (4.2) as I desire; $a = 0.10$ produces the best-fitting hyperbola. Figure 7 shows this

265   result.

266   Conceptually, we can use (4.3) to predict spray concentration if we can associate a wind

267   speed dependence for the spectra plotted in Figs. 5 and 6. All we need to know is how

268    $C_0(r_0 = 6.25 \mu\text{m})$, the concentration for droplets in the bin centered at 6.25 µm used to

269   nondimensionalized the spectra in Fig. 7, depends on wind speed.

270   To evaluate this wind speed dependence, I first looked at the wind speed dependence of

271   all the concentration data because any wind speed dependence that I assign to the 6.25-µm radius

272   bin must be appropriate for all radius bins up to 143.75 µm. Figure 8 therefore plots normalized

273   droplet concentrations from all 333 droplet spectra. I calculated these normalized concentrations

274   by dividing all concentrations in a specific radius bin by the average concentration for that bin.

275   Consequently, the normalized concentrations in Fig. 8 tend to distribute equally below and above

276   one.

277   I fitted straight lines through the log-log data in Fig. 8. The standard approach is to do

278   least-squares linear regression with y as the dependent variable and x as the independent variable.

279   When both x and y have comparable uncertainties, however, such a fitting can be biased because

280   least-squares algorithms presume that the x values are perfectly known. Consequently, I also like

281   to derive a fitting relation from the bisector of y-versus-x and x-versus-y least-squares fits (e.g.,

282   Andreas 2002a). Figure 8 also shows this bisector fit. Lastly, since both fitting lines are close to

283   cubic in wind speed, Fig. 8 shows the cubic relation for which the normalized concentration goes

284   as U_{N10}^3.

285   In Fig. 8, the cubic relation splits the *y*-versus-*x* and bisector fits and, by eye, does best at

286   representing the data for all radius bins and for all wind speeds. I thus represent the

287   concentration data for the 6.25-μm radius bin with a cubic relation in U_{N10}. Figure 9 shows that

288   representation, which is

289
$$C_0\left(r_0=6.25\,\mu\text{m}\right) = 100.38U_{N10}^3. \tag{4.4}$$

290   This gives $C_0(r_0 = 6.25\ \mu\text{m})$ in $\text{m}^{-3}\ \mu\text{m}^{-1}$ for U_{N10} in m s^{-1}.

291   I close the discussion of Fig. 8 by pointing out, again, that the data collected during high

292   water do not differ appreciably from the data collected during low water.

293   Combining (4.4) and (4.3) produces an expression to fit the near-surface spray

294   concentrations measured on Mt. Desert Rock:

295
$$C_0\left(r_0, U_{N10}\right) = 100.38U_{N10}^3 \exp\Big[-4.20022$$
$$-4.08587\Big\{\big[\ln\left(r_0\right) - 4.10051\big] + \big\{0.29891\big[\ln\left(r_0\right) - 4.10051\big]^2 + 0.0078383\big\}^{1/2}\Big\}\Big]. \tag{4.5}$$

296   Again, C_0 is in $\text{m}^{-3}\ \mu\text{m}^{-1}$ when U_{N10} is in m s^{-1} and r_0 is in μm.

297   With the green curves, each panel in Figs. 5 and 6 displays (4.5), where U_{N10} for each

298   green curve is taken as the mid-range wind speed for the wind speed range indicated in the panel.

299   I draw two conclusions from these green curves. First, the shape of the droplet spectra is

300   consistent for all the wind speeds depicted. Second, the cubic dependence on U_{N10} does well in

301   representing the spectral levels at all wind speeds in the dataset.

302

303 **5. Spray generation function**

304 The spray generation function, which I henceforth denote as dF/dr_0 (e.g., Monahan et al.

305 1986; Andreas 2002b), predicts the number of spray droplets with initial radius r_0 that are

306 produced per square meter of sea surface per second per micrometer increment in droplet radius.

307 Its units are thus $m^{-2}\ s^{-1}\ \mu m^{-1}$, where r_0 is expressed in micrometers.

308 Often, dF/dr_0 is calculated as the near-surface droplet concentration, $C_0(r_0)$, times some

309 velocity scale (e.g., Moore and Mason 1954; Fairall and Larsen 1984; Smith et al. 1993; Lewis

310 and Schwarz 2004, p. 101; Hoppel et al. 2005; de Leeuw et al. 2011). This approach makes the

311 reasonable assumption that, to be observed, spray droplets need some upward velocity to be

312 entrained in the air flow. Andreas et al. (2010) evaluated the usefulness of this approach for four

313 distinct velocity scales—the dry deposition velocity, which can be close to the terminal fall

314 velocity; a turbulent droplet diffusion velocity; the jet droplet ejection velocity; and the wind

315 speed evaluated at the significant wave amplitude, $U_{A_{1/3}}$. For the droplets like those observed at

316 Mt. Desert Rock—with radii of about 10 μm and larger—Andreas et al. concluded that $U_{A_{1/3}}$ is

317 the best velocity scale for predicting spray generation from the near-surface concentration.

318 Therefore, I estimate the spray generation function as

$$319 \qquad \frac{dF}{dr_0} = U_{A_{1/3}} C_0\left(r_0, U_{N10}\right), \qquad (5.1)$$

320 where C_0 comes from (4.5).

321 Figure 10 shows this spray generation function for a range of wind speeds. Finding U_{N10}

322 and $U_{A_{1/3}}$ values to use in (5.1) is crucial. To compute these, I first run the new bulk flux

323 algorithm that Andreas et al. (2015) describe; from sea surface temperature (T_s) and from wind

324 speed (U_r), air temperature (T_a), and relative humidity (RH_r) at arbitrary reference height r, it

14

325   computes, among other quantities, the friction velocity u_* and the Obukhov length L. Equations

326   like (3.1) and (3.2) yield $U_{A_{1/3}}$ and U_{N10} as

327
$$U_{A_{1/3}} = U_r + \frac{u_*}{k}\left[\ln\left(\frac{A_{1/3}}{r}\right) - \psi_m\left(\frac{A_{1/3}}{L}\right) + \psi_m\left(\frac{r}{L}\right)\right]$$
(5.2)

328   and

329
$$U_{N10} = U_r + \frac{u_*}{k}\ln\left(\frac{10}{r}\right).$$
(5.3)

330   For comparison with an open ocean spray generation function, I also plot in Fig. 10 the

331   function that Andreas et al. (2010) created by smoothly joining the bubbles-only function from

332   Monahan et al. (1986) with the large-radius function that Fairall et al. (1994) formulated from an

333   earlier function from Andreas (1992). After reviewing the field, Andreas (2002b) had concluded

334   that the Monahan et al. function provides an "anchor" for predicting the generation of small

335   droplets over the open ocean while the Fairall et al. function has the best overall properties for

336   high winds and larger droplets.

337   Furthermore, the merging is fairly easy: Both functions take as their wind speed

338   dependence the whitecap coverage (W) that Monahan and O'Muircheartaigh (1980) deduced,

339
$$W(U_{10}) = 3.8 \times 10^{-6} U_{10}^{3.4}.$$
(5.4)

340   In this, W is the fractional whitecap coverage, and U_{10} is the wind speed at 10 m.

341   In Fig. 10, (5.1) is roughly three orders of magnitude larger than the joint Monahan and

342   Fairall function for droplets smaller than about 30 μm in radius. As the radius increases, this

343   difference decreases until the level of (5.1) extrapolated to $r_0 = 200$ μm is very close to the level

344   of the joint Monahan and Fairall function. The large-radius slope of my new function is also

345   very close to the large-radius slope of the Monahan and Fairall function.

15

346 Previously, de Leeuw et al. (2000) measured surf zone production at the Scripps pier in

347 La Jolla, California. Likewise, van Eijk et al. (2011) measured surf zone production at La Jolla

348 and also at the Field Research Facility in Duck, North Carolina. Both of these surf zones are

349 characterized by gently sloping beaches in contrast to the abrupt, rocky shoreline and the absence

350 of a beach at Mt. Desert Rock. de Leeuw et al. concluded that the breaking waves at the La Jolla

351 site enhanced spray production by up to two orders of magnitude. For their two sites, van Eijk et

352 al. concluded that the surface zone added 0.7 to one order of magnitude to the spray

353 concentration. Remember, though, both groups observed spray droplets with radii no bigger than

354 30 μm.

355 The next section continues this discussion of the enhanced spray production that I

356 observed.

357

358   **6. Discussion**

359   *a. Footprint analysis*

360   The explanation for the magnitude of the spray flux observed at Mt. Desert Rock is

361   intimately tied to the upwind footprint that influenced measurements at the cloud imaging probe.

362   Classically, the flux footprint is a function of distance (x) upwind from an instrument, which is at

363   height z_m; the origin of this distance is at the instrument. By integrating over all x the surface

364   flux at location x multiplied by the footprint function at x, we derive the flux at the origin and at

365   height z_m that the instrument sees (e.g., Horst and Weil 1992, 1994; Wilson 2015).

366   Besides z_m, which is 3.24 m for the cloud imaging probe, another parameter that is

367   important in most footprint analyses is the aerodynamic roughness length z_0. For a typical wind

368   speed in my dataset, 12 m s^{-1}, I estimate $z_0 = 3.4 \times 10^{-4}$ m . Hence, z_m/z_0, another important

369   quantity, is about 9500. The height of the atmospheric boundary layer, h, and the ratio z_m/h are

370   also required in some footprint analyses. Without measurements of h, I surmise that it was rarely

371   less than 400 m; therefore, $z_m/h \leq 0.008$.

372   The footprint function is zero for some distance immediately upwind of the instrument

373   (Horst and Weil 1994; Hsieh et al. 2000; Wilson 2015). In essence, material escaping the

374   surface too close to the instrument does not have time to reach height z_m and be observed before

375   it is blown beyond the instrument. I denote this distance X for "excluded."

376   The total upwind extent of the flux footprint itself I denote as F (in meters). From figures

377   in Kljun et al. (2004; e.g., Fig. 1), I estimate that, for the given values of z_m, z_0, h, and

378   stratification, the footprint is approximately zero for F larger than about 200 m. In other words,

379   the CIP is most sensitive to the surface within 200 m upwind from it. Meanwhile, the peak of

380   the footprint function—the region of upwind fetch that contributes the most to observations at

381   height z_m—is roughly 50–70 m upwind of the instrument (Horst and Weil 1994, Fig. 3; Kljun et

382   al., Fig. 1). From Fig. 1, we can therefore conclude that most of the spray reaching the cloud

383   imaging probe originated in or near the surf zone.

384   Let us suppose that this surf zone has a width S. But S is not constant; I observed it to

385   increase with wind speed (and the resulting wave energy) such that it was about 30 m wide for

386   the highest wind speeds we encountered on Mt. Desert Rock, about 20 m s^{-1}. As a crude

387   estimate to model this wind speed effect on the surf zone, I use

388
$$S = 30\left(\frac{U_{N10}}{20}\right)^3,$$
(6.1)

389   where S is in meters when U_{N10} is in m s^{-1}. This choice of a cubic dependence on U_{N10}

390   recognizes that the energy flux that the wind puts into the ocean—and which, in turn, builds the

391   waves that create the surf zone—scales with the cube of the wind speed (e.g., Wu 1979).

392   With this conceptual framework, I can predict how the quantity of spray produced in a

393   surf zone might differ from spray over the open ocean. Over the open ocean, the spray measured

394   by a cloud imaging probe at height z_m would scale something like

395
$$\text{Ocean:} \quad W\left(U_{10}\right)\left(F - X\right).$$
(6.2)

396   The spray actually measured by the CIP at Mt. Desert Rock, on the other hand, would scale like

397
$$\text{MDR:} \quad W\left(U_{10}\right)\left(F - S - R\right) + 1 \cdot \gamma \cdot S + 0 \cdot R.$$
(6.3)

398   Both of these equations rest on the common practice of inferring spray production from whitecap

399   coverage.

400   In (6.2) and (6.3), $W(U_{10})$ is the fractional whitecap coverage for the open ocean as

401   estimated from (5.4). In (6.3), R is the distance over rock from the CIP to the shoreline on Mt.

402   Desert Rock; I estimate it as, typically, 30 m (see Fig. 1). This portion of the footprint obviously

18

403   produces no spray; the footprint function is thus zero here. In contrast, the surface zone is one

404   continuously renewed whitecap; the fractional whitecap coverage is 1 here (de Leeuw et al.

405   2000; i.e., the 1 multiplying the S term in (6.3)). Moreover, as I will discuss shortly, the surf

406   zone is more productive white water than would be characterized by just whitecap coverage,

407   (5.4). Therefore, I include the γ coefficient in the S term and expect γ to be one or greater.

408   By taking the ratio of (6.3) to (6.2), we can estimate how productive the surf zone at Mt.

409   Desert Rock is compared to the open ocean:

410
$$Ratio = \frac{W(U_{10})(F - S - R) + \gamma S}{W(U_{10})(F - X)}. \tag{6.4}$$

411   For demonstration purposes and because R and X are relatively small compared to F, I set $X = R$.

412   Then (6.4) reduces to

413
$$Ratio = \frac{\gamma S}{W(U_{10})(F - R)} + 1 - \frac{S}{F - R}. \tag{6.5}$$

414   The white water in the surf zone more closely resembles a stage A whitecap than a stage

415   B whitecap. Stage A whitecaps are associated with actively breaking waves, while stage B

416   whitecaps result from the rising, decaying bubble plumes left after a wave breaks (Monahan and

417   Lu 1990). The surf zone at Mt. Desert Rock during winds of 10 m s^{-1} and higher was a very

418   energetic and turbulent region of total white water and continually breaking waves (cf. Brocchini

419   and Peregrine 2002).

420   Woolf et al. (1987) and Cipriano et al. (1987) studied spray formation in a laboratory

421   whitecap simulation tank. Although they could measure only spray droplets with radii of about

422   10 μm or less, their result are, nevertheless, suggestive of what we might see on Mt. Desert

423   Rock. Figures 4 and 5 in Woolf et al. and Fig. 2 in Cipriano et al. suggest that a newly formed

424   whitecap (the stage A whitecap) produces about an order of magnitude more spray droplets per

425 unit time than the later decaying phase (stage B) of the whitecap. On reevaluating these papers,

426 Ed Monahan (2015, personal communication) estimated that the production of these droplets,

427 which have radii at the small end of my spectrum, may even be up to two orders of magnitude

428 higher in stage A whitecaps than in stage B whitecaps.

429   These studies by Woolf et al. (1987) and Cipriano et al. (1987) generally quantified only

430 the spray production by bursting bubbles—that is, film and jet droplets. In the surf zone, with an

431 onshore wind, other mechanisms can also create spray droplets (e.g., Peregrine 1983; Monahan

432 et al. 1986; Andreas et al. 1995, Fig. 1; Brocchini and Peregrine 2002). Spume droplets, which

433 the wind tears right off the wave crests (e.g., Soloviev et al. 2012), are generally larger than film

434 and jet droplets. In the very turbulent surf zone, where waves reflected from the steep shore

435 collide with incoming waves from the ocean, so-called splash and chop droplets also occur. It is

436 therefore not implausible to speculate that these latter processes, especially, can enhance the

437 spray production another order of magnitude.

438   In summary, spray production in a surf zone at a rocky shoreline, where white water is

439 ubiquitous and continually renewed, could be 10 to 1000 times higher at comparable winds

440 speeds than over the open ocean, where spray production predominantly comes from stage A and

441 stage B whitecaps. Therefore, Fig. 11 displays the ratio in (6.5) for γ ranging from 1 to 1000.

442   Although their geometry was somewhat different than for my observations on Mt. Desert

443 Rock, the $\gamma = 1$ and $\gamma = 10$ cases in Fig. 11 approximate the data that de Leeuw et al. (2000) and

444 van Eijk et al. (2011) obtained downwind of far less energetic surf zones over sloping beaches.

445 Even if the breakers on their beaches were not more effective spray producers than open ocean

446 whitecaps—that is, assuming $\gamma = 1$—Fig. 11 suggests that the spray production would still be

447 enhanced by a factor of 3 or 4 because of the increased whitecap coverage.

448   Meanwhile, according to Fig. 11, a γ value between 100 and 1000—which according to

449   my literature review seems to be possible—would explain the observed spray concentrations and

450   spray generation function (Fig. 10), where the Mt. Desert Rock values are about three orders of

451   magnitude larger than over the open ocean.

452

453   *b. Parameterizing the spray*

454   The debate on how to parameterize near-surface spray concentration and the spray

455   generation function has gone back and forth for about 35 years. One approach assumes that the

456   shape of the spray distribution with radius at formation r_0 is independent of forcing variables like

457   wind speed, wave field, or water temperature. Then the near-surface spray concentration (as a

458   function of just radius and wind speed for demonstration purposes) could be formulated as the

459   product of a shape function, $f(r_0)$, and a forcing function, $g(U_{10})$:

460    $$C_0\left(r_0, U_{10}\right) \;=\; f\left(r_0\right) g\left(U_{10}\right). \tag{6.6}$$

461   de Leeuw et al. (2011) reviewed this concept; and it has found application in spray generation

462   functions formulated by Monahan et al. (1986, their bubbles-only function), Fairall et al. (1994),

463   and Andreas et al. (2010), among others.

464   The second school of thought supposes that the shape of the droplet spectrum depends on

465   the forcing variables; and, therefore, separating the size function and the forcing function as in

466   (6.6) is not possible. Monahan et al. (1983) seemed to document this change in the droplet

467   spectrum with wind speed when they observed enhanced droplet counts for large droplets at

468   higher wind speeds. Miller and Fairall (1988) put this approach in practice when they

469   synthesized from four datasets a spray generation function for which the shape changed with

470   wind speed. Andreas (1992), for example, was an early user of this Miller and Fairall function.

21

471   Smith et al. (1993) and later Smith and Harrison (1998) likewise derived spray generation

472   functions for which the shape of the droplet spectrum changed with wind speed.

473   My observations, however, come down on the side of (6.6)—that the droplet spectrum

474   does not change shape significantly with wind speed or other forcing variables for wind speeds

475   between 5 and 17 m s^{-1}. In view of Figs. 5, 6, and 7, this conclusion is very robust.

476   Admittedly, the references cited in this section were all to open ocean conditions. Hence,

477   it is not clear that the data from Mt. Desert Rock can be extended to the open ocean and, thereby,

478   can add weight to either side of the argument on how to parameterize C_0 and dF/dr_0. I,

479   nevertheless, felt it essential to interpret my data in the context of this debate.

480

481   *c. Height profile of the spray*

482   To assess icing and sea salt accumulation on structures downwind of a shoreline where

483   spray is forming, we need to model the profile of the spray as a function of vertical coordinate *z*.

484   Equations that have appeared earlier provide the solution. Namely, we can rearrange (3.5) to get

485   the spray concentration profile:

486
$$C\left(z, r_0, U_{N10}\right) \,=\, C_0\left(r_0, U_{N10}\right) \left(\frac{z}{A_{1/3}}\right)^{-V_g(r_0)/k u_* f_s} . \tag{6.7}$$

487   Furthermore, we can substitute (4.5) for $C_0(r_0, U_{N10})$. Equation (3.6) shows how to calculate f_s.

488   To continue with the calculation, readers can use their favorite algorithms for computing

489   V_g and u_*. Alternatively, they can retrieve from

490   http://people.nwra.com/resumes/andreas/software.php a bulk flux algorithm that Andreas et al.

491   (2015) developed for computing u_* over the ocean, among other fluxes, and a second algorithm

492   for fast microphysical calculations that include computing V_g (Andreas 2005).

493

494 **7. Conclusions**

495   With increasing wind speed, the surf zone at the rocky shore of Mt. Desert Rock became

496 increasingly energetic. Active wave breaking, ubiquitous stage A whitecaps, and continuous

497 turbulent white water grew oceanward from the shoreline with increasing winds. A cloud

498 imaging probe placed a few tens of meters downwind from this surf zone counted the spray

499 droplets generated there.

500   For 10-m, neutral-stability wind speeds (U_{N10}) between 5 and 17 m s^{-1}, I thus documented

501 the near-surface concentration of spray droplets in 12 12.5-μm-wide bins with centers from 6.25

502 to 143.75 μm. One of the main results is that the shape of these near-surface concentration

503 spectra, $C_0(r_0, U_{N10})$, as a function of droplet radius at formation, r_0, is independent of wind

504 speed. I could, thus, formulate an expression for the near-surface concentration in terms of two

505 independent functions:

506
$$C_0\left(r_0, U_{10}\right) = f\left(r_0\right)g\left(U_{10}\right), \tag{7.1}$$

507 where $f(r_0)$ is a shape function and $g(U_{N10})$ is a wind speed function. Equations (4.3) and (4.4),

508 respectively, give these two functions.

509   Because of the high energy in the surf zone and the fact that a footprint analysis suggests

510 that the cloud imaging probe focused preferentially on spray coming from the surf zone, the

511 measured spray concentrations are two to three orders of magnitude higher than those measured

512 over the open ocean. Waves crashing against rocks also produce one to two orders of magnitude

513 more spray than waves breaking on sloping beaches.

514   The spray generation function derived from these near-surface concentration

515 measurements reiterates how much more productive the surf zone is than is the open ocean.

516 Figure 10 shows that, at least for droplets smaller than about 30 μm in r_0, the surf zone at Mt.

23

517   Desert Rock was three orders of magnitude more productive than the open ocean.

518   For droplets above 100 µm in radius, on the other hand, the Mt. Desert Rock spray

519   generation function is comparable to the open ocean function. There are two possible

520   explanations for this convergence for large radii. Either the joint Monahan et al. (1986) and

521   Fairall et al. (1994) function overestimates the generation rate of the largest droplets or, at the

522   CIP site on Mt. Desert Rock, many of the larger droplets settled out of the air flow before the

523   CIP could count them. Both explanations are plausible because the counting statistics for the

524   CIP were best for the smaller droplets, while the joint Monahan and Fairall function for open

525   ocean spray generation shown in Fig. 10 is also most reliable for the smaller droplets. In

526   summary, the orders-of-magnitude difference in spray concentration and in spray generation

527   (Fig. 10) between Mt. Desert Rock and the open ocean is robust for droplet radii less than 50–

528   100 µm.

529   Because these observations on Mt. Desert Rock are the first spray measurements at a

530   rocky shoreline, I cannot say how general the results are. The footprint analysis in Section 6a

531   provides justification for presuming that production in the surf zone at a rocky shoreline should

532   be 2–3 orders of magnitude higher than over the open ocean. Moreover, its correct order-of-

533   magnitude prediction for spray production over a sloping, sandy beach provides validation for

534   that analysis. Consequently, although (4.5) and (5.1) may not be perfectly transferrable to other

535   abrupt shores, they should be useful planning tools for evaluating how hazardous spray icing and

536   sea salt might be for artificial islands currently built or planned for the high-latitude ocean.

537

546

APPENDIX

Obtaining Droplet Concentration from the Cloud Imaging Probe

549   The cloud imaging probe (CIP; from Droplet Measurement Technologies, Inc., Boulder,

550   Colorado) uses single-particle optical imaging with a linear array of 64 photodetectors to count

551   and size droplets. The following equations that I used to process the raw CIP data come from the

552   user's manuals (Anonymous 2009, 2012) and from software that Chris Fairall (2012, personal

553   communication) shared with me.

554   The CIP uses a red laser; the wavelength is $\lambda = 0.660$ μm. The resolution in size bins is

555     $R = 25$ μm: that is, the CIP counts droplets in size bins that increase from zero in steps of 25 μm

556   in diameter. The CIP has a linear array of 64 (= ND) diode detectors; it thus can sort droplets

557   into 62 (= NB) bins, each 25-μm wide.

558   I do the analysis, however, in terms of droplet radius; thus, the radius resolution is

559     $\Delta r = R/2 = 12.5$ μm. With 62 CIP bins of width Δr, the upper radius limit for each bin (Bin_{Hi})

560   increases as $12.5i$, where $i = 1,62$. Hence, $Bin_{Hi} = 12.5, 25, 37.5, 50, \ldots, 762.5, 775$ μm.

561   Likewise, the lower limit on each radius bin (Bin_{Lo}) goes as $12.5(i - 1)$, where $i = 1,62$. That is,

562     $Bin_{Lo} = 0, 12.5, 25, 37.5, \ldots, 750, 762.5$ μm. My convention is to use the center radius of each

563   bin to denote droplets counted by the CIP at a given radius. The center radius of a bin (in μm) is

564     $Bin_{cent} = 6.25 + 12.5(i - 1)$, where $i = 1,62$.

565   On Mt. Desert Rock, the counting statistics for 30 minutes of sampling were poor for

566   droplets beyond the bin centered at 143.75 μm. Hence, my plots show only droplets centered in

567   the 12 bins 6.25, 18.75, 31.25, 43.75, …, 131.25, 143.75 μm.

568   Approximately every second, the CIP reported the number of droplets counted in each of

569   its 62 bins. Call this one-second value the count K in bin i at time j, $K(j,i)$. The number of

570   droplets counted in bin i in 30 minutes is simply the sum of all these counts:

$$\overline{K}(i) = \sum_{j=1}^{\sim1800} K(j,i). \tag{A1}$$

572   To find the droplet concentration in bin i for the 30 minutes, we must divide the bin sum

573   by the total volume of air sampled (V) and by the bin width, Δr:

$$C(i) = \frac{\overline{K}}{V \Delta r}. \tag{A2}$$

575   This has units of a droplet concentration: number of droplets per cubic meter of air per

576   micrometer increment in droplet radius.

577   The volume V depends on the size bin. We first calculate the length of the diode array

578   for droplets of size i:

$$L_{CIP}(i) = 2 \cdot 0.001 \cdot \Delta r (ND - i - 1), \tag{A3}$$

580   where $i = 1,62$ and the 0.001 converts Δr in micrometers to millimeters. Thus, the lengths of the

581   bins are $L_{CIP}(1) = 1.550$ mm, $L_{CIP}(2) = 1.525$ mm, $L_{CIP}(3) = 1.500$ mm, …, $L_{CIP}(61) = 0.050$ mm,

582   $L_{CIP}(62) = 0.025$ mm.

583   The second length scale is the distance across the laser array, $zz(i)$. Again, this distance is

584   a function of size bin but also of the laser optics. From Chris Fairall (2012, personal

585   communication),

$$zz(i) = \min\left\{1580\,DOF0\left[0.001\,Bin_{Hi}(i)\right]^2, 100\,\text{mm}\right\}, \tag{A4}$$

587   where zz is also in millimeters and $Bin_{Hi}(i)$ is the upper radius limit of the ith bin.

588   $DOF0 = 2.4054$ is related to the depth of field of the laser array. Equation (A4) gives

589   $zz(1) = 0.594$ mm, $zz(2) = 2.375$ mm, $zz(3) = 5.344$ mm, …, $zz(12) = 85.51$ mm,

590   $zz(13) = 100$ mm. And for all higher bins, zz is also 100 mm.

591   The final dimension for calculating the volume V in (A2) is related to the flow of air

592   through the laser array. This is just $\overline{U}_{\perp}\Delta t$, where $\overline{U}_{\perp}$ is the average wind speed perpendicular

593   to the laser array during the 30-minute sampling (or sometimes shorter) period (Δt) as measured

594   by the Gill sonic anemometer attached to the cloud imaging probe. I made no corrections for the

595   sonic's being 48 cm above the laser array.

596   Putting this last result together with (A3) and (A4) in (A2), I finish the algorithm for

597   computing the spray droplet concentration in bin i:

598
$$C(i) = \frac{10^{6}\,\overline{K}_{i}}{L_{CIP}(i)\,zz(i)\,\overline{\overline{U}}_{\perp}\,\Delta t\,\Delta r}.\qquad\text{(A5)}$$

599   Because L_{CIP} and zz are both expressed in millimeters, we must multiply the right side of (A5) by

600   10^{6} to obtain $C(i)$ in $\text{m}^{-3}\,\mu\text{m}^{-1}$.

601

REFERENCES

Andreas, E. L, 1992: Sea spray and the turbulent air-sea heat fluxes. *J. Geophys. Res.*, **97,** 11429–11441.

—, 2002a: Parameterizing scalar transfer over snow and ice: A review. *J. Hydrometeor.*, **3,** 417–432.

—, 2002b: A review of the sea spray generation function for the open ocean. *Atmosphere-Ocean Interactions*, Vol. 1, W. Perrie, Ed., WIT Press, 1–46.

—, 2005: Approximation formulas for the microphysical properties of saline droplets. *Atmos. Res.*, **75,** 323–345.

—, and S. Wang, 2007: Predicting significant wave height off the northeast coast of the United States. *Ocean Eng.*, **34,** 1328–1335.

—, J. B. Edson, E. C. Monahan, M. P. Rouault, and S. D. Smith, 1995: The spray contribution to net evaporation from the sea: A review of recent progress. *Bound.-Layer Meteor.*, **72,** 3–52.

—, K. F. Jones, and C. W. Fairall, 2010: Production velocity of sea spray droplets. *J. Geophys. Res.*, **115,** C12065, doi:10.1029/2010JC006458.

—, L. Mahrt, and D. Vickers, 2012: A new drag relation for aerodynamically rough flow over the ocean. *J. Atmos. Sci.*, **69,** 2520–2537.

—, —, and —, 2015: An improved bulk air-sea surface flux algorithm, including spray-mediated transfer. *Quart. J. Roy. Meteor. Soc.*, **141,** 642–654.

Anonymous, 2009: Data analysis user's guide. Chapter II: Single particle imaging. DOC-0223, Rev A, Droplet Measurement Technologies, Inc., Boulder, CO, 34 pp.

624 ____, 2012: Cloud imaging probe (CIP). Manual DOC-0028, Rev L, Droplet Measurement

625 Technologies, Inc., Boulder, CO, 66 pp.

626 Asplin, M. G., R. Galley, D. G. Barber, and S. Prinsenberg, 2012: Fracture of summer perennial

627 sea ice by ocean swell as a result of Arctic storms. *J. Geophys. Res.*, **117,** C06025,

628 doi:10.1029/2011JC007221.

629 Brocchini, M., and D. H. Peregrine, 2002: The dynamics of strong turbulence at free surfaces.

630 Part 1. Description. *Advances in Coastal and Ocean Engineering, Vol. 8: Interaction of*

631 *Strong Turbulence with Free Surfaces*, M. Brocchini and D. H. Peregrine, Eds., World

632 Scientific, 1–41.

633 Cipriano, R. J., E. C. Monahan, P. A. Bowyer, and D. K. Woolf, 1987: Marine condensation

634 nucleus generation inferred from whitecap simulation tank results. *J. Geophys. Res.*, **92,**

635 6569–6576.

636 Clarke, A. D., S. R. Owens, and J. Zhou, 2006: An ultrafine sea-salt flux from breaking waves:

637 Implications for cloud condensation nuclei in the remote marine atmosphere. *J. Geophys.*

638 *Res.*, **111,** D06202, doi:10.1029/2005JD006565.

639 de Leeuw, G., F. P. Neele, M. Hill, M. H. Smith, and E. Vignati, 2000: Production of sea spray

640 aerosol in the surf zone. *J. Geophys. Res.*, **105,** 29397–29409.

641 ____, E. L Andreas, M. D. Anguelova, C. W. Fairall, E. R. Lewis, C. O'Dowd, M. Schulz, and

642 S. E. Schwartz, 2011: Production flux of sea spray aerosol. *Rev. Geophys.*, **49,** RG2001,

643 doi:10.1029/2010RG000349.

644 Fairall, C. W., and S. E. Larsen, 1984: Dry deposition, surface production and dynamics of

645 aerosols in the marine boundary layer. *Atmos. Environ.*, **18,** 69–77.

646   ____, J. D. Kepert, and G. J. Holland, 1994: The effect of sea spray on surface energy transports

647   over the ocean. *Global Atmos. Ocean Syst.*, **2,** 121–142.

648   ____, M. L. Banner, W. L. Peirson, W. Asher, and R. P. Morison, 2009: Investigation of the

649   physical scaling of sea spray spume droplet production. *J. Geophys. Res.*, **114,** C10001,

650   doi:10.1029/2008JC004918.

651 Gerwick, B. C., Jr., 2007: *Construction of Marine and Offshore Structures*. CRC Press, 813 pp.

652 Hoppel, W. A., P. F. Caffrey, and G. M. Frick, 2005: Particle deposition on water: Surface

653   source versus upwind source. *J. Geophys. Res.*, **110,** D10206,

654   doi:10.1029/2004JD005148.

655 Horst, T. W., and J. C. Weil, 1992: Footprint estimation for scalar flux measurements in the

656   atmospheric surface layer. *Bound.-Layer Meteor.*, **59,** 279–296.

657   ____, and ____, 1994: How far is far enough?: The fetch requirements for micrometeorological

658   measurement of surface fluxes. *J. Atmos. Oceanic Technol.*, **11,** 1018–1025.

659 Hsieh, C.-I, G. Katul, and T.-W. Chi, 2000: An approximate analytical model for footprint

660   estimation of scalar fluxes in thermally stratified atmospheric flows. *Adv. Water Resour.*,

661   **23,** 765–772.

662 Itagaki, K., 1984: Icing rate on stationary structures under marine conditions. CRREL Rep.

663   84-12, U.S. Army Cold Regions Research and Engineering Laboratory, 9 pp.

664 Jones, K. F., and E. L Andreas, 2009: Sea spray icing of drilling and production platforms.

665   ERDC/CRREL Tech. Rep. TR-09-3, U.S. Army Cold Regions Research and Engineering

666   Laboratory, 54 pp.

667   ____, and ____, 2012: Sea spray concentrations and the icing of fixed offshore structures.

668   *Quart. J. Roy. Meteor. Soc.*, **138,** 131–144.

669　　　Kaimal, J. C., and J. J. Finnigan, 1994: *Atmospheric Boundary Layer Flows: Their Structure*

670　　　　　　*and Measurement.* Oxford University Press, 289 pp.

671　　　Kepert, J., C. Fairall, and J.-W. Bao, 1999: Modelling the interaction between the atmospheric

672　　　　　　boundary layer and evaporating sea spray droplets. *Air-Sea Exchange: Physics,*

673　　　　　　*Chemistry and Dynamics*, G. L. Geernaert, Ed., Kluwer, 363–409.

674　　　Kljun, N., P. Calanca, M. W. Rotach, and H. P. Schmid, 2004: A simple parameterisation for

675　　　　　　flux footprint predictions. *Bound.-Layer Meteor.*, **112,** 503–523.

676　　　Lewis, E. R., and S. E. Schwartz, 2004: *Sea Salt Aerosol Production: Mechanisms, Methods,*

677　　　　　　*Measurements, and Models—A Critical Review.* American Geophysical Union, 413 pp.

678　　　Miller, M. A., and C. W. Fairall, 1988: A new parameterization of spray droplet production by

679　　　　　　oceanic whitecaps. Preprints, *Seventh Conf. on Ocean-Atmosphere Interaction*,

680　　　　　　Anaheim, CA, Amer. Meteor. Soc., 174–177.

681　　　Minsk, L. D., 1984a: Ice observation program on the semisubmersible drilling vessel *SEDCO*

682　　　　　　*708*. CRREL Special Rep. 84-2, U.S. Army Cold Regions Research and Engineering

683　　　　　　Laboratory, 14 pp.

684　　　——, 1984b: Assessment of ice accretion on offshore structures. CRREL Special Rep. 84-4,

685　　　　　　U.S. Army Cold Regions Research and Engineering Laboratory, 12 pp.

686　　　Monahan, E. C., and M. Lu, 1990: Acoustically relevant bubble assemblages and their

687　　　　　　dependence on meteorological parameters. *IEEE J. Oceanic Eng.*, **15,** 340–349.

688　　　——, and I. O'Muircheartaigh, 1980: Optimal power-law description of oceanic whitecap

689　　　　　　coverage dependence on wind speed. *J. Phys. Oceanogr.*, **10,** 2094–2099.

690   ____, C. W. Fairall, K. L. Davidson, and P. J. Boyle, 1983: Observed inter-relations between

691   10 m winds, ocean whitecaps and marine aerosols. *Quart. J. Roy. Meteor. Soc.*, **109,**

692   379–392.

693   ____, D. E. Spiel, and K. L. Davidson, 1986: A model of marine aerosol generation via

694   whitecaps and wave disruption. *Oceanic Whitecaps and Their Role in Air-Sea Exchange*

695   *Processes*, E. C. Monahan and G. Mac Niocaill, Eds., D. Reidel, 167–174.

696   Moore, D. J., and B. J. Mason, 1954: The concentration, size distribution and production rate of

697   large salt nuclei over the oceans. *Quart. J. Roy. Meteor. Soc.*, **80,** 583–590.

698   Muzik, I., and A. Kirby, 1992: Spray overtopping rates for Tarsiut Island: Model and field

699   study results. *Can. J. Civ. Eng.*, **19,** 469–477

700   Nauman, J. W., 1984: Superstructure icing observations on the semisubmersible *Ocean Bounty*

701   in lower Cook Inlet, Alaska. Proc., *Second International Workshop on Atmospheric Icing*

702   *of Structures*, Trondheim, Norway, 71–79.

703   Panofsky, H. A., and J. A. Dutton, 1984: *Atmospheric Turbulence: Models and Methods for*

704   *Engineering Applications*. John Wiley and Sons, 397 pp.

705   Peregrine, D. H., 1983: Breaking waves on beaches. *Annu. Rev. Fluid Mech.*, **15,** 149–178.

706   Perrie, W., and Coauthors, 2012: Selected topics in Arctic atmosphere and climate. *Climatic*

707   *Change*, **115,** 35–58.

708   Piazzola, J., G. Tedeschi, and A. Demoisson, 2015: A model for the transport of sea-spray

709   aerosols in the coastal zone. *Bound.-Layer Meteor.*, **155,** 329–350.

710   Rouault, M. P., P. G. Mestayer, and R. Schiestel, 1991: A model of evaporating spray droplet

711   dispersion. *J. Geophys. Res.*, **96,** 7181–7200.

712   Smith, M. H., and N. M. Harrison, 1998: The sea spray generation function. *J. Aerosol Sci.*, **29,**

713   Suppl. 1, S189–S190.

714   ____, P. M. Park, and I. E. Consterdine, 1993: Marine aerosol concentrations and estimated

715   fluxes over the sea. *Quart. J. Roy. Meteor. Soc.*, **119,** 809–824.

716   Soloviev, A., A. Fujimura, and S. Matt, 2012: Air-sea interface in hurricane conditions. *J.*

717   *Geophys. Res.*, **117,** C00J34, doi:10.1029/2011JC007760.

718   van Eijk, A. M. J., J. T. Kusmierczyk-Michulec, M. J. Francius, G. Tedeschi, J. Piazolla, D. L.

719   Merritt, and J. D. Fontana, 2011: Sea-spray aerosol particles generated in the surf zone.

720   *J. Geophys. Res.*, **116,** D19210, doi:10.1029/2011JD015602.

721   Vignati, E., G. de Leeuw, and R. Berkowicz, 2001: Modeling coastal aerosol transport and

722   effects of surf-produced aerosols on processes in the marine atmospheric boundary layer.

723   *J. Geophys. Res.*, **106,** 20225–20338.

724   Wilson, J. D., 2015: Computing the flux footprint. *Bound.-Layer Meteor.*, **156,** 1–13.

725   Woolf, D. K., P. A. Bowyer, and E. C. Monahan, 1987: Discriminating between the film drops

726   and jet drops produced by a simulated whitecap. *J. Geophys. Res.*, **92,** 5142–5150.

727   Wu, J., 1979: Oceanic whitecaps and sea state. *J. Phys. Oceanogr.*, **9,** 1064–1068.

728

CAPTIONS OF FIGURES

730   FIG. 1. Mt. Desert Rock. The light gray shading is the island at high tide; the dark gray, the

731   island at low tide. The range between high and low tide is about 3 m. Orange objects are

732   permanent structures: The oval is the lighthouse; the big square is the lightkeeper's house. The

733   red circle on the small square is the cloud imaging probe and associated sonic

734   anemometer/thermometer mounted on the foghorn platform. The three-legged symbol denotes

735   the "turbulence tripod." The quadrant 260° to 7° indicates the only wind directions I retained for

736   my analyses. The arcs at 50 and 75 m show that all samples collected by the cloud imaging

737   probe were within 75 m of the water; and, at high tide, most were much closer.

738   FIG. 2. The cloud imaging probe from Droplet Measurement Technologies and the Gill sonic

739   anemometer/thermometer mounted on the foghorn platform on Mt. Desert Rock.

740   FIG. 3. Wind speed, air temperature, and relative humidity during the experiment on Mt. Desert

741   Rock (MDR). All legends refer to all panels. "MDR NOAA" identifies the NOAA instruments

742   on the lighthouse; likewise, "Matinicus" denotes the NOAA instruments on Matinicus Rock.

743   "Gill Sonic on MDR" is wind speed from the Gill sonic anemometer associated with the cloud

744   imaging probe. "Our Data" identifies the wind speed and temperature data from the turbulence

745   tripod.

746   FIG. 4. Surface water temperature and salinity and significant wave height ($H_{1/3}$) during the

747   experiment on Mt. Desert Rock. In the temperature and salinity panels, the data identified as

748   "Ours" are from manual bucket samples. In the wave height panel, our estimate of $H_{1/3}$ comes

749   from the Andreas and Wang (2007) algorithm and the wind speed from the Gill sonic

750   anemometer.

751   FIG. 5. Near-surface spray droplet concentration spectra (i.e., C_0 from (3.5)) for wind speeds

752   (U_{N10}) between 6 and 10 m s^{-1}. The black and red curves distinguish between measurements

753   made during high water and low water, respectively. The green curve is the fit to these

754   concentration spectra, (4.5), where the U_{N10} used to calculate each green curve is the middle

755   value of the indicated wind speed range.

756   FIG. 6. As in Fig. 5 but for wind speeds between 10 and 17 m s^{-1}.

757   FIG. 7. All the concentration spectra (e.g., Figs. 5 and 6) measured in wind speeds (U_{N10}) of

758   5 m s^{-1} and higher are nondimensionalized with the respective concentration measured in the

759   radius bin centered at 6.25 µm. Hence, all spectra are identically one for $r_0 = 6.25$ µm. The plot

760   still distinguishes measurements made during high water from those made during low water.

761   The plot also shows the bin medians for all the data and, individually, for the high-water and

762   low-water data. The small-radius bins and the large-radius bins fall along straight lines in this

763   log-log plot (the two black lines). I thus represent the median nondimensional spectrum with a

764   hyperbola, (4.3) with $a = 0.10$.

765   FIG. 8. All concentration data in the 333 runs are normalized and plotted against U_{N10}. The

766   normalization is for each radius bin such that all concentrations measured in that bin are divided

767   by the bin average. The data are identified as to whether they were collected during high water

768   or low water. Three fitting lines are shown: one calculated using least-squares linear regression

769   as y-versus-x, one taken as the bisector of y-versus-x and x-versus-y fits, and one for which a

770   U_{N10}^3 dependence is assumed.

771 FIG. 9. The near-surface spray concentration data (i.e., C_0) for the bin centered at $r_0 = 6.25$ μm

772 are plotted versus the neutral-stability wind speed at 10 m, U_{N10}. The blue line is the best-fitting

773 cubic relation through these data, (4.4).

774 FIG. 10. The Mt. Desert Rock (MDR) spray generation function, (5.1), as a number flux for

775 various values of the wind speed at a reference height of 10 m, U_{10}. For these calculations, the

776 surface temperature (T_s) was 1°C; the air temperature (T_r), 0°C; the relative humidity (RH_r),

777 80%; the surface salinity, 34 psu; and the barometric pressure, 1000 mb. For comparison, the

778 plot also shows the joint Monahan et al. (1986) and Fairall et al. (1994) function (from Andreas

779 et al. 2010).

780 FIG. 11. The ratio of surf-zone production to open-ocean production of spray, as predicted by

781 (6.5), is plotted as a function of 10-m wind speed (U_{10}) for the γ values indicated. As explained

782 in the text, in (6.5) $F = 200$ m, $R = 30$ m, S comes from (6.1), and $W(U_{10})$ comes from (5.4).

37
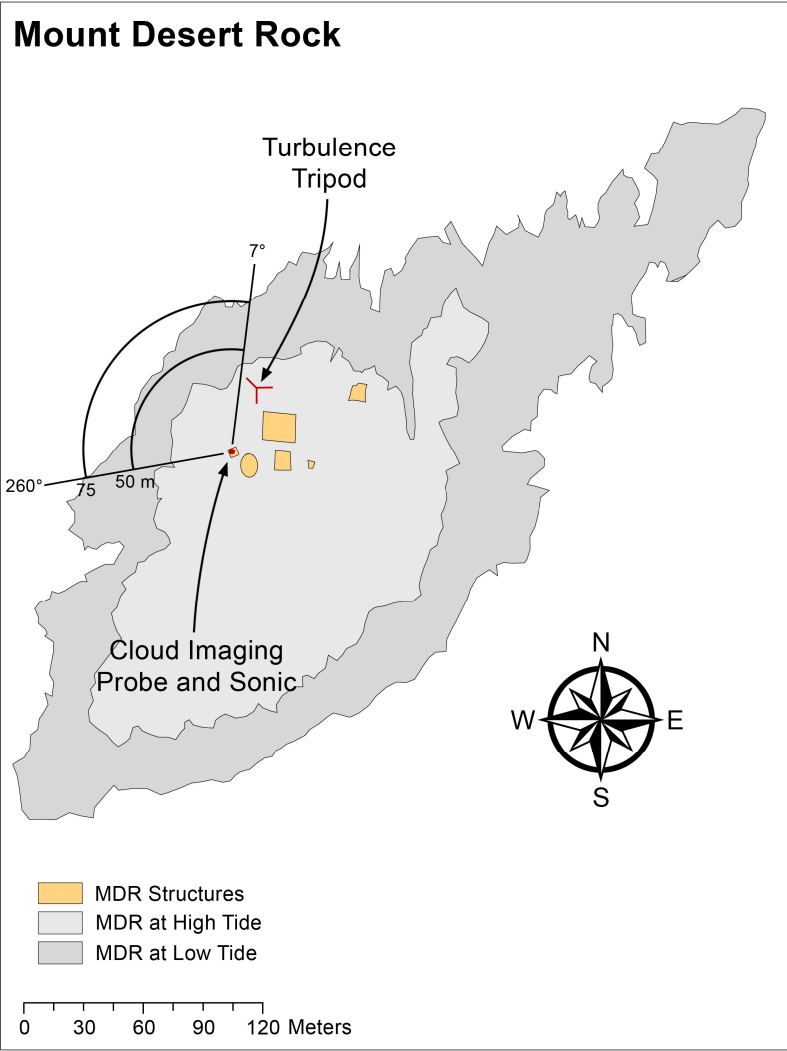
Mount Desert Rock

FIG. 1. Mt. Desert Rock. The light gray shading is the island at high tide; the dark gray, the island at low tide. The range between high and low tide is about 3 m. Orange objects are permanent structures: The oval is the lighthouse; the big square is the lightkeeper's house. The red circle on the small square is the cloud imaging probe and associated sonic anemometer/thermometer mounted on the foghorn platform. The three-legged symbol denotes the "turbulence tripod." The quadrant 260° to 7° indicates the only wind directions I retained for my analyses. The arcs at 50 and 75 m show that all samples collected by the cloud imaging probe were within 75 m of the water; and, at high tide, most were much closer.

785

FIG. 2. The cloud imaging probe from Droplet Measurement Technologies and the Gill sonic anemometer/thermometer mounted on the foghorn platform on Mt. Desert Rock.

786
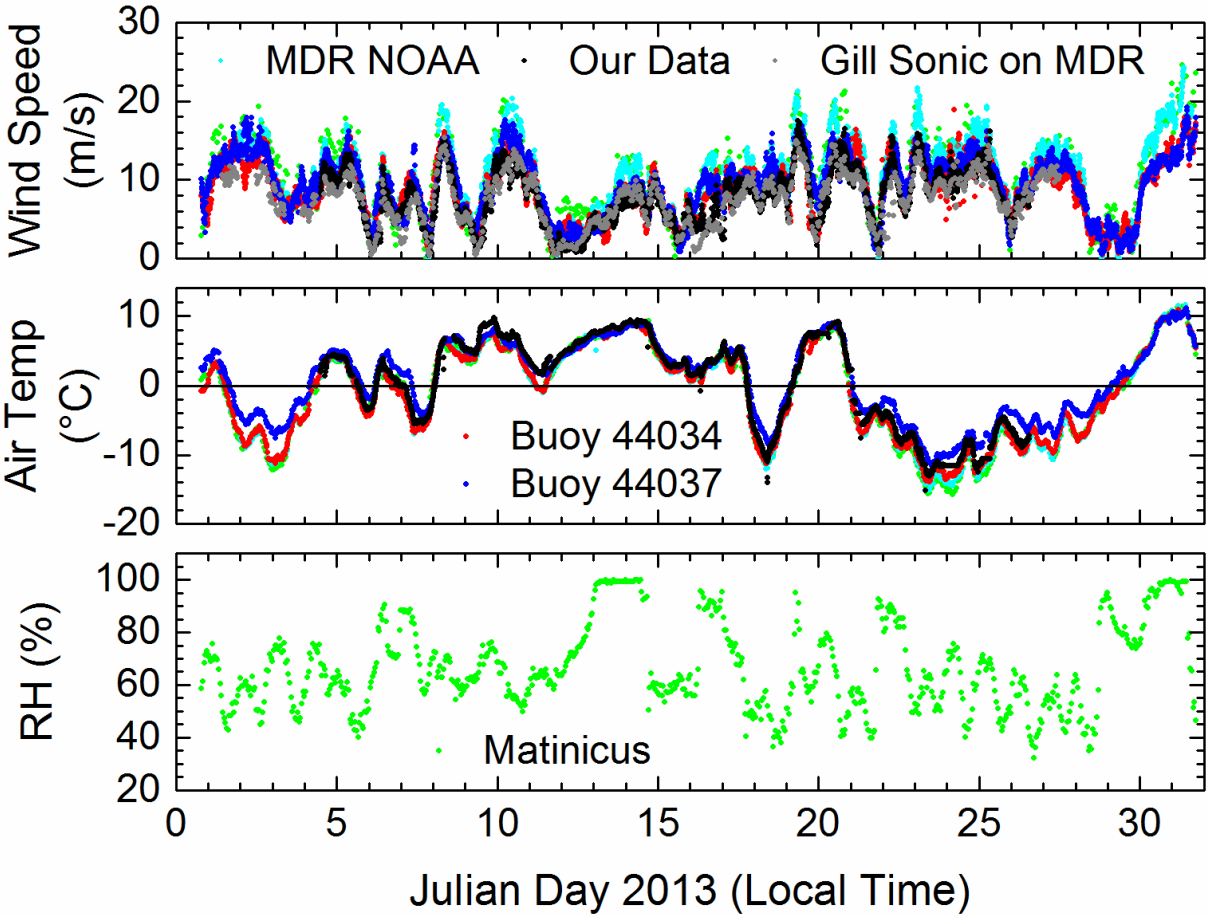
FIG. 3. Wind speed, air temperature, and relative humidity during the experiment on Mt. Desert Rock (MDR). All legends refer to all panels. "MDR NOAA" identifies the NOAA instruments on the lighthouse; likewise, "Matinicus" denotes the NOAA instruments on Matinicus Rock. "Gill Sonic on MDR" is wind speed from the Gill sonic anemometer associated with the cloud imaging probe. "Our Data" identifies the wind speed and temperature data from the turbulence tripod.
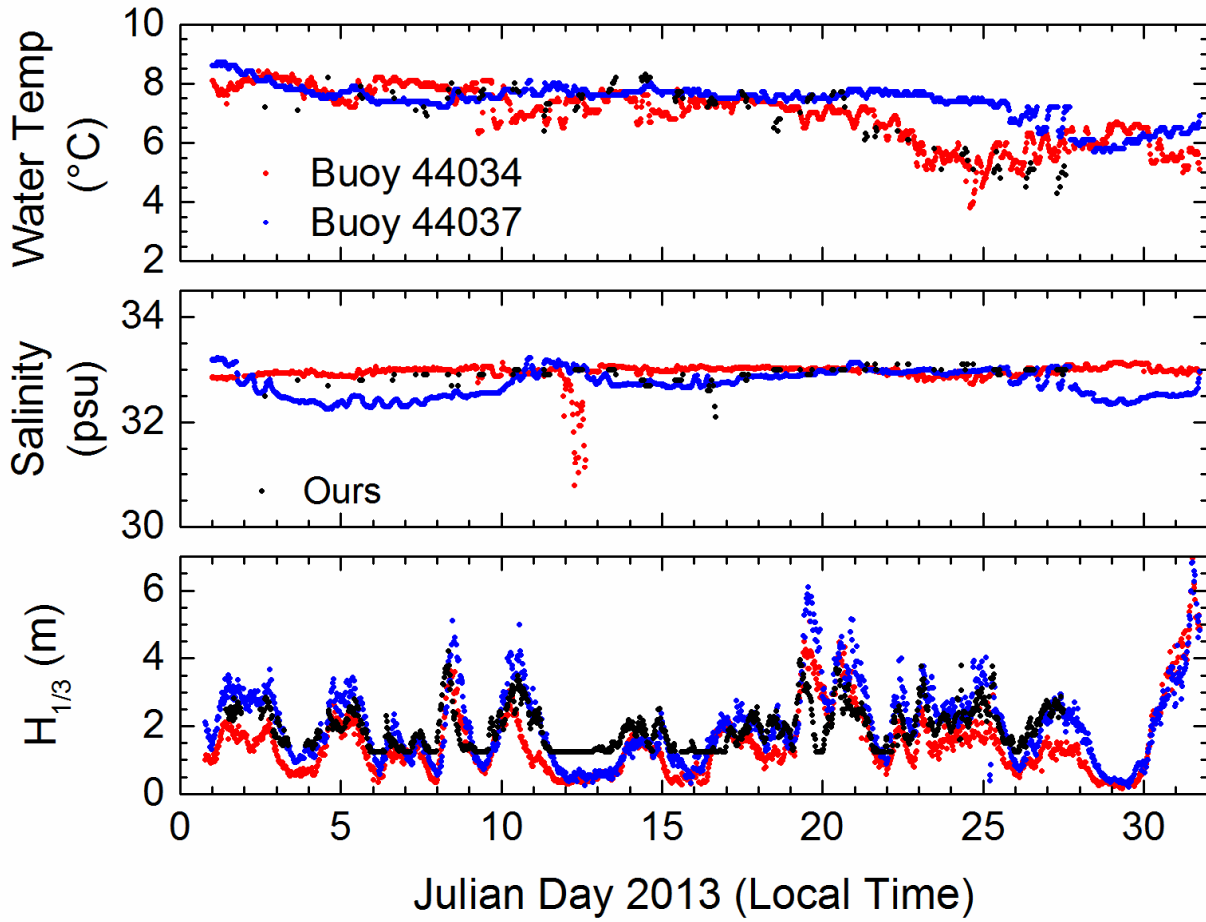
FIG. 4. Surface water temperature and salinity and significant wave height ($H_{1/3}$) during the experiment on Mt. Desert Rock. In the temperature and salinity panels, the data identified as "Ours" are from manual bucket samples. In the wave height panel, our estimate of $H_{1/3}$ comes from the Andreas and Wang (2007) algorithm and the wind speed from the Gill sonic anemometer.
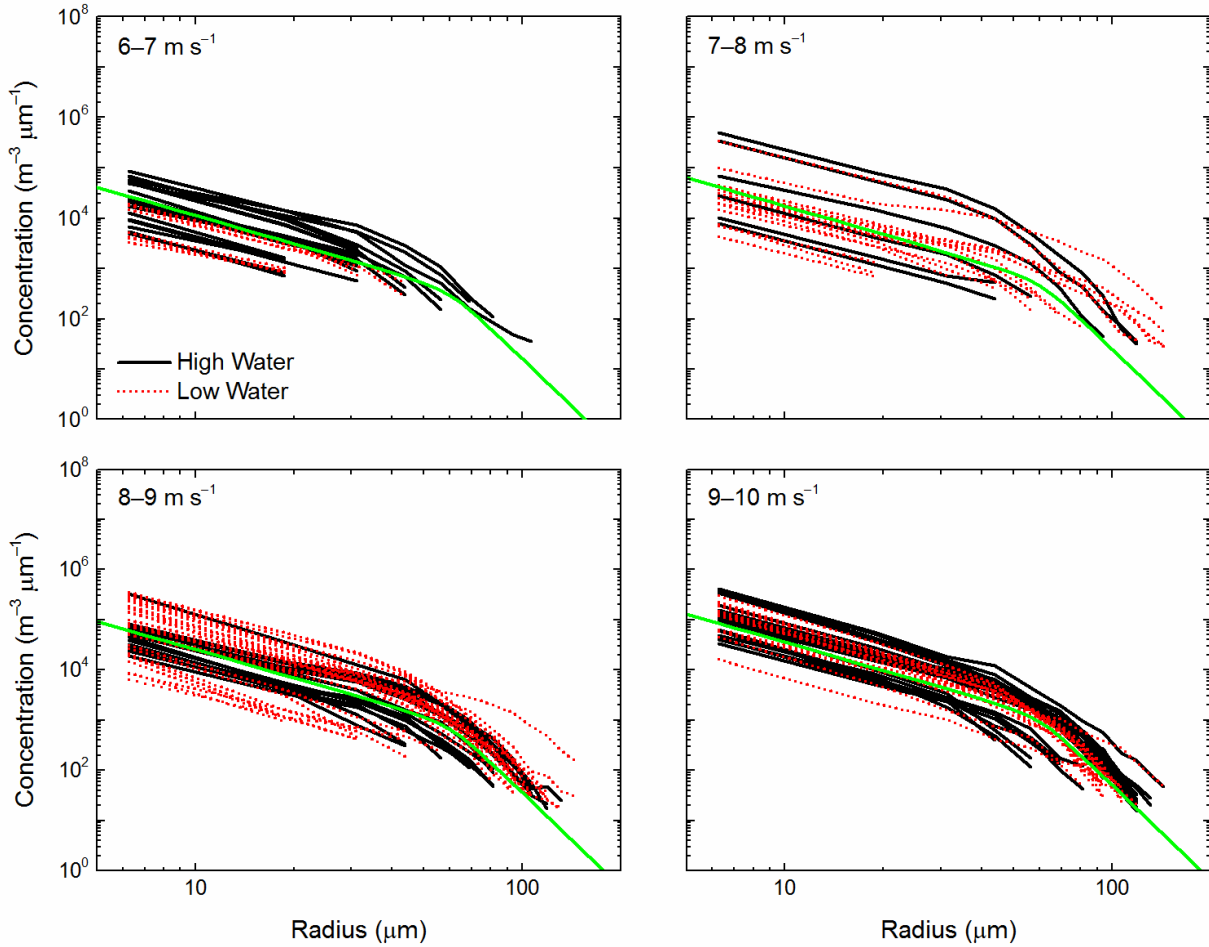
FIG. 5. Near-surface spray droplet concentration spectra (i.e., C_0 from (3.5)) for wind speeds (U_{N10}) between 6 and 10 m s^{-1}. The black and red curves distinguish between measurements made during high water and low water, respectively. The green curve is the fit to these concentration spectra, (4.5), where the U_{N10} used to calculate each green curve is the middle value of the indicated wind speed range.
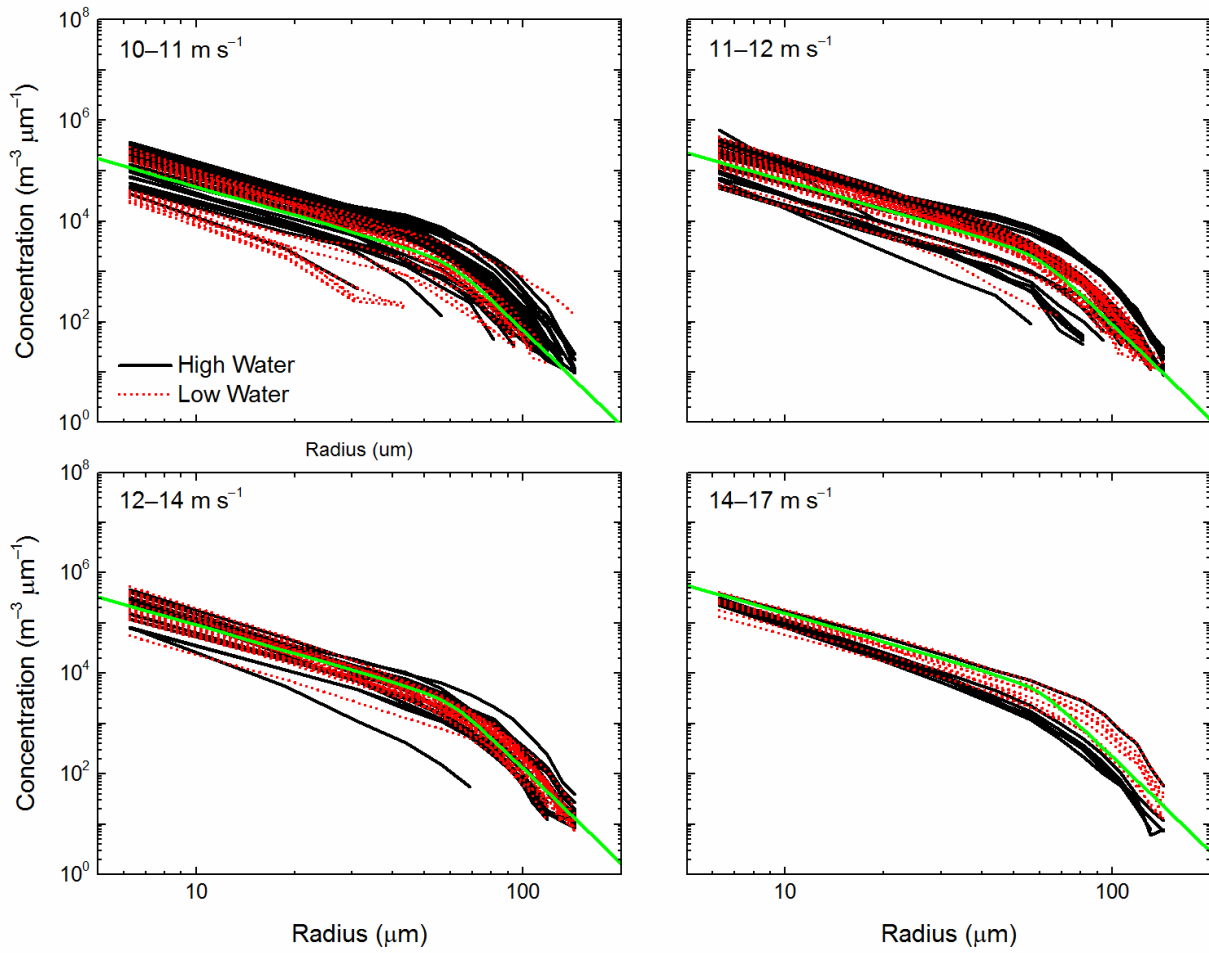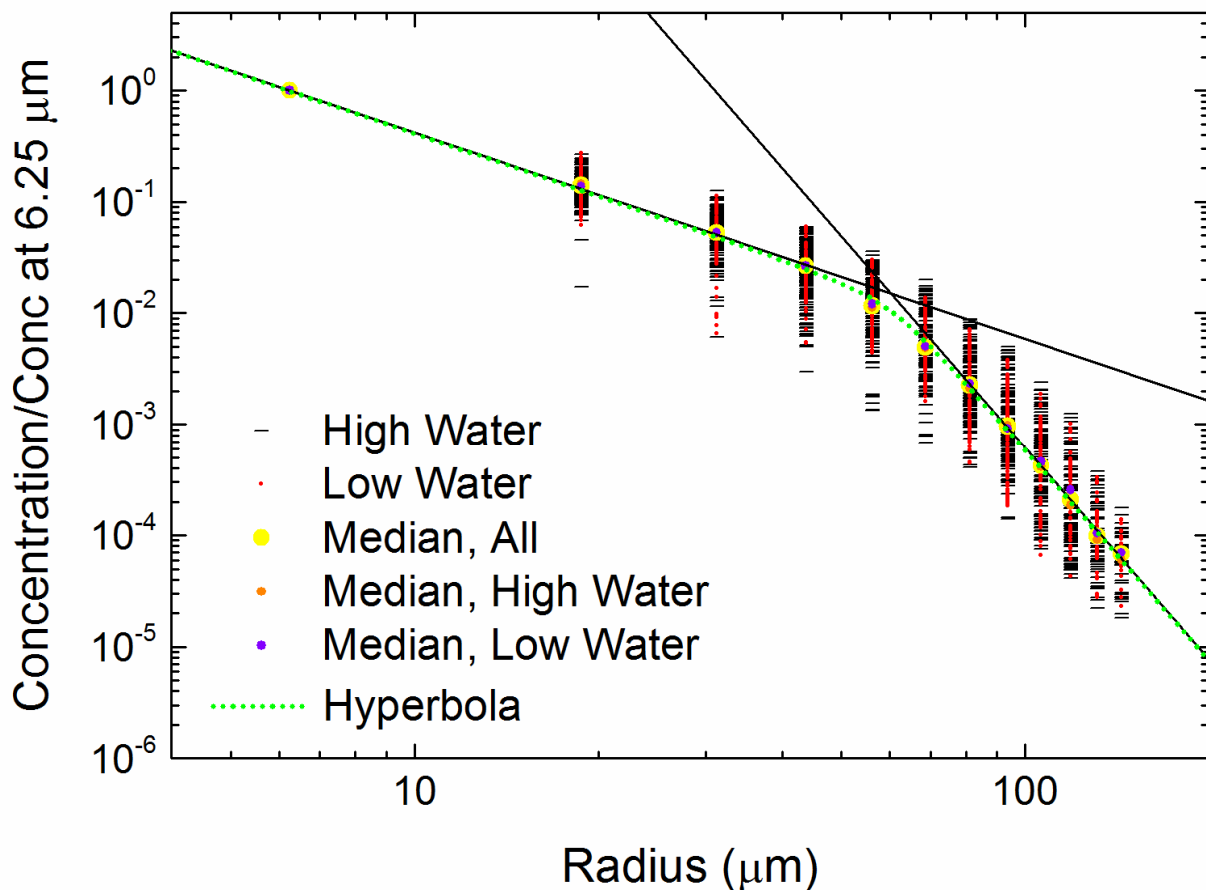
FIG. 6. As in Fig. 5 but for wind speeds between 10 and 17 m s^{-1}.

FIG. 7. All the concentration spectra (e.g., Figs. 5 and 6) measured in wind speeds (U_{N10}) of

5 m s^{-1} and higher are nondimensionalized with the respective concentration measured in the

radius bin centered at 6.25 μm. Hence, all spectra are identically one for $r_0 = 6.25$ μm. The plot

still distinguishes measurements made during high water from those made during low water.

The plot also shows the bin medians for all the data and, individually, for the high-water and

low-water data. The small-radius bins and the large-radius bins fall along straight lines in this

log-log plot (the two black lines). I thus represent the median nondimensional spectrum with a
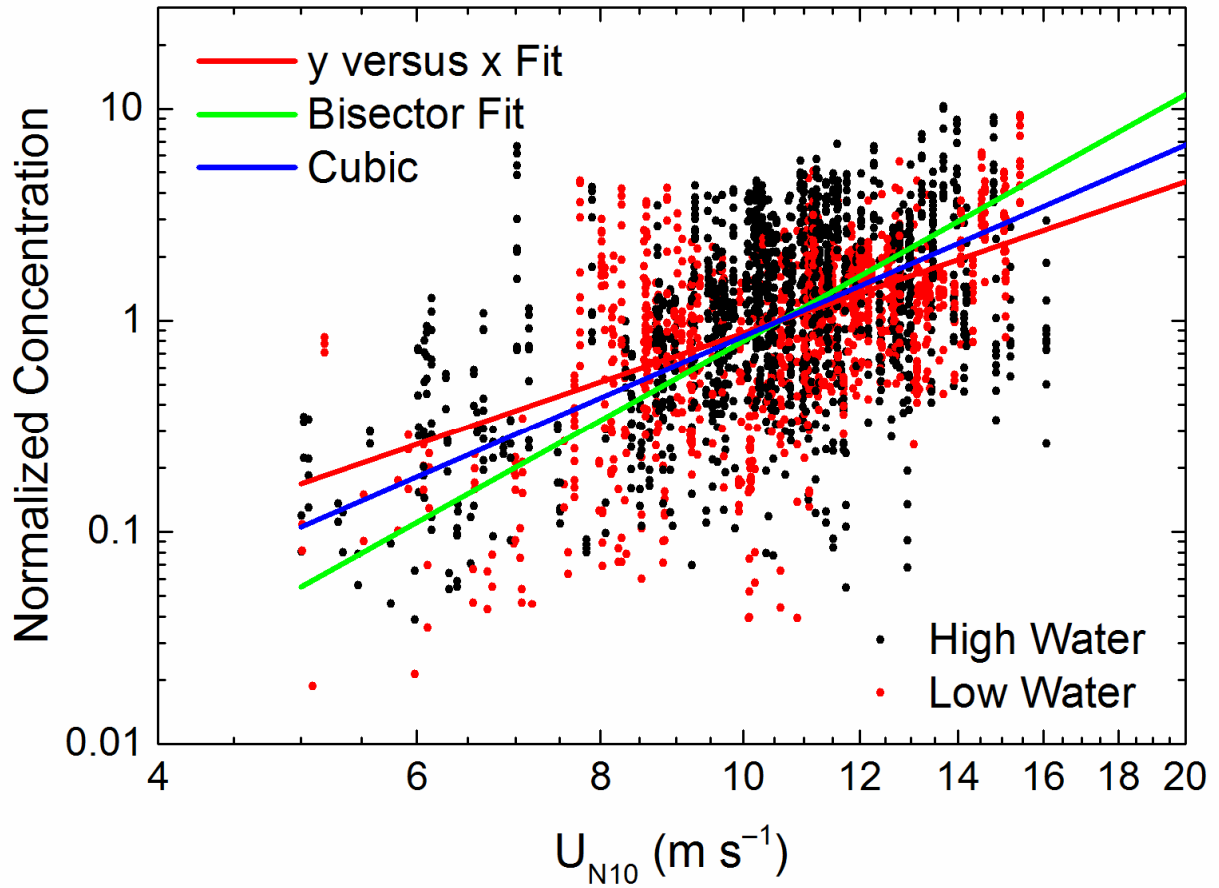
hyperbola, (4.3) with $a = 0.10$.

FIG. 8. All concentration data in the 333 runs are normalized and plotted against U_{N10}. The normalization is for each radius bin such that all concentrations measured in that bin are divided by the bin average. The data are identified as to whether they were collected during high water or low water. Three fitting lines are shown: one calculated using least-squares linear regression as *y-versus-x*, one taken as the bisector of *y-versus-x* and *x-versus-y* fits, and one for which a U_{N10}^3 dependence is assumed.
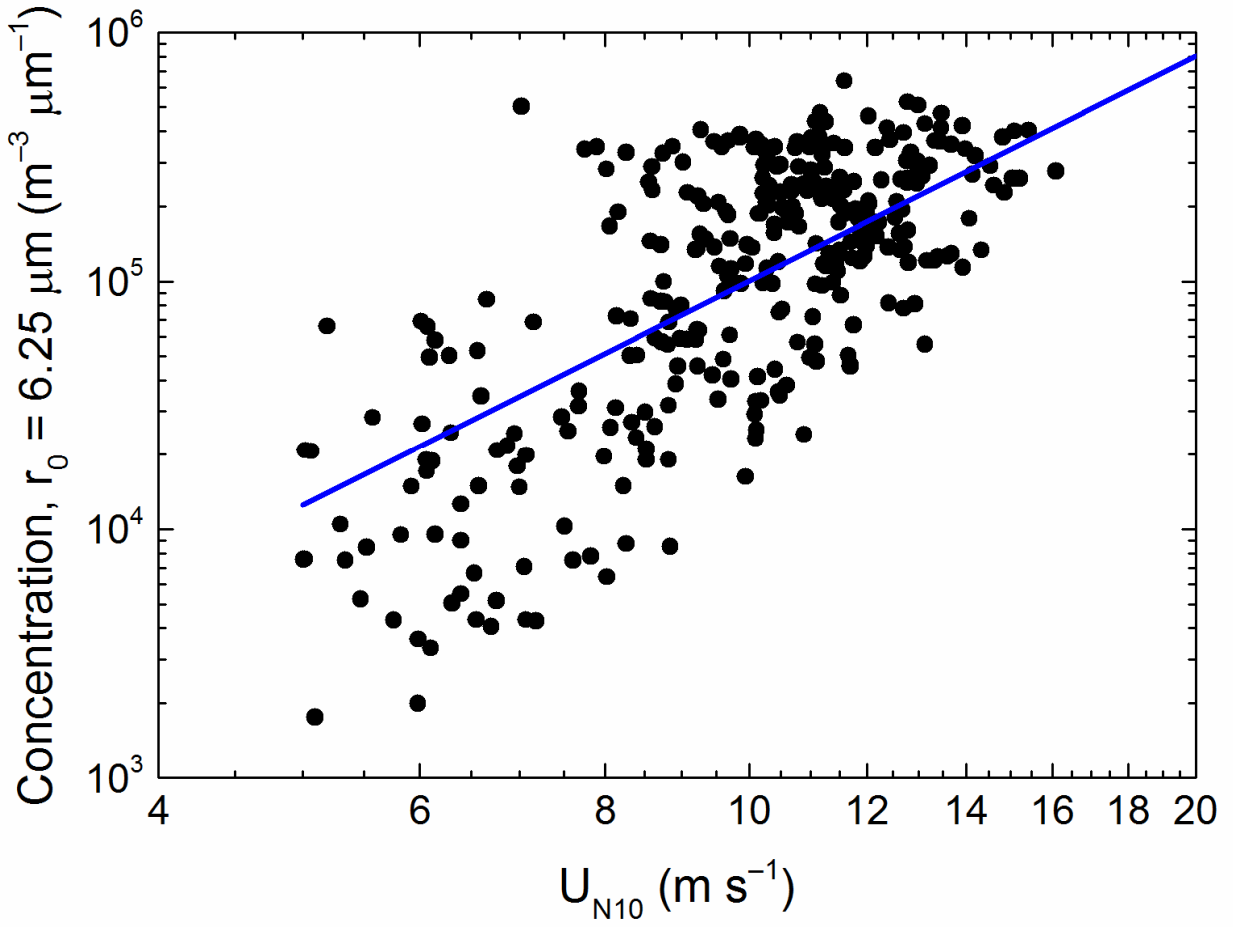
FIG. 9. The near-surface spray concentration data (i.e., C_0) for the bin centered at $r_0 = 6.25$ μm are plotted versus the neutral-stability wind speed at 10 m, U_{N10}. The blue line is the best-fitting cubic relation through these data, (4.4).
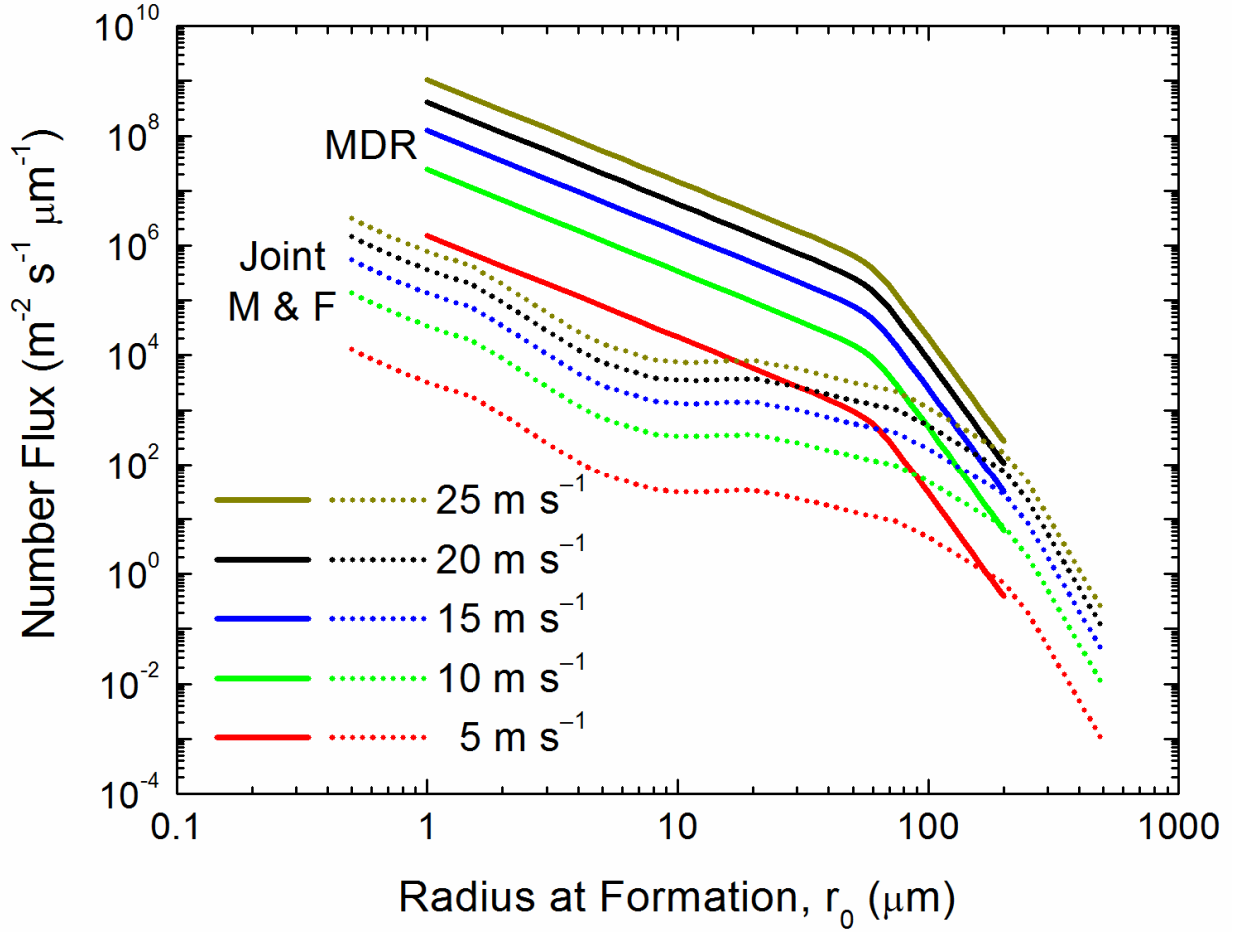
801

FIG. 10. The Mt. Desert Rock (MDR) spray generation function, (5.1), as a number flux for various values of the wind speed at a reference height of 10 m, U_{10}. For these calculations, the surface temperature (T_s) was 1°C; the air temperature (T_r), 0°C; the relative humidity (RH_r), 80%; the surface salinity, 34 psu; and the barometric pressure, 1000 mb. For comparison, the plot also shows the joint Monahan et al. (1986) and Fairall et al. (1994) function (from Andreas et al. 2010).
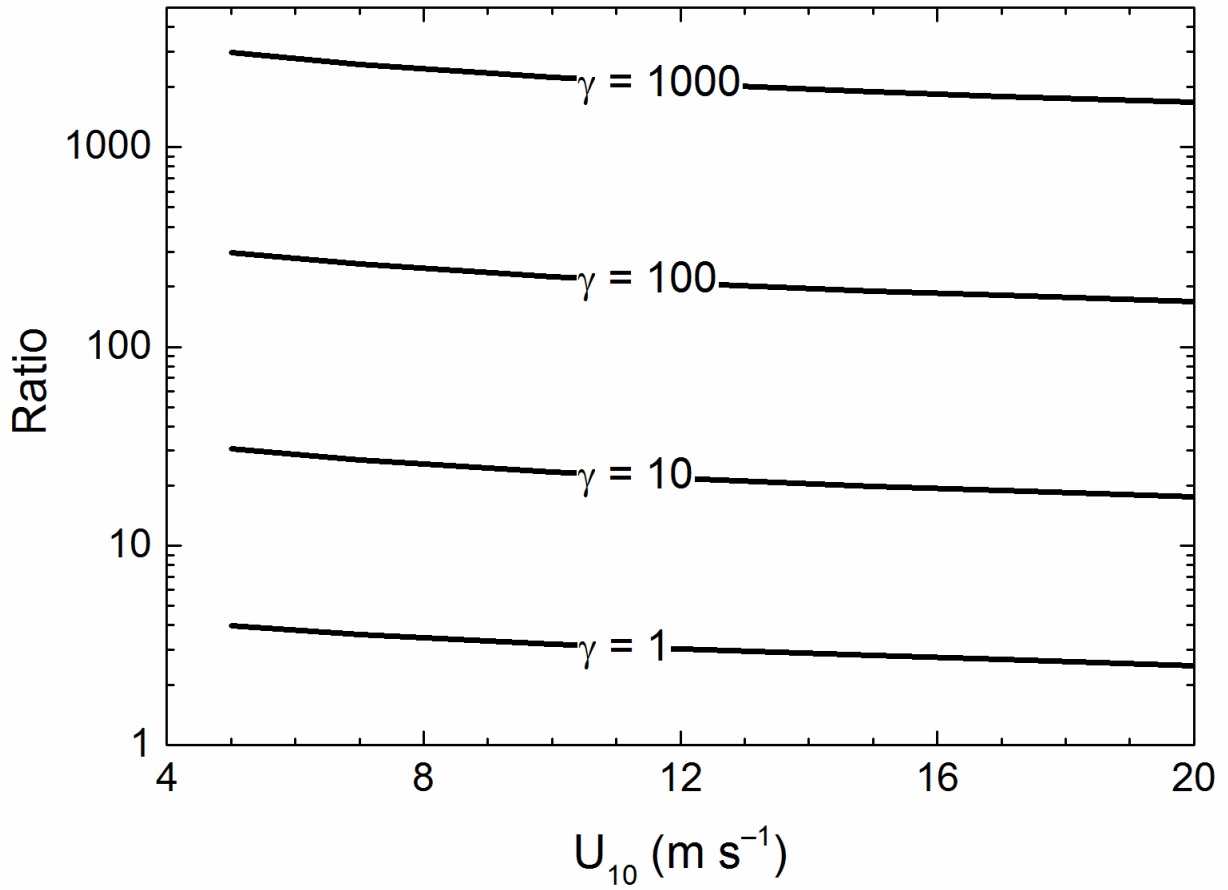
802

803

FIG. 11. The ratio of surf-zone production to open-ocean production of spray, as predicted by

(6.5), is plotted as a function of 10-m wind speed (U_{10}) for the γ values indicated. As explained

in the text, in (6.5) $F = 200$ m, $R = 30$ m, S comes from (6.1), and $W(U_{10})$ comes from (5.4).

804

48